ORIGINAL ARTICLE

A boundary-based fourier neural operator (B-FNO) method for efficient parametric acoustic wave analysis

Ruoyan Li[1,2] · Wenjing Ye[1] · Yijun Liu[2]

Abstract

Repetitive wave analysis is required in various applications involving parametric analyses across different settings. However, traditional numerical methods based on domain discretization become computationally impractical due to the large number of simulations required, especially in unbounded domains. The boundary element method (BEM) is known for its effectiveness in solving wave equations, particularly in unbounded domains. Nevertheless, even with accelerated techniques, large-scale problems and those with high frequencies often necessitate numerous iterations, hampered by ill-conditioned system matrices. As a result, BEM becomes unsuitable for parametric analysis. To address these challenges, surrogate modelling techniques have been developed, and recent advancements in neural operators show promise in constructing surrogate models. However, they still face limitations when efficiently handling exterior and high-dimensional problems. In this study, we propose a novel data-driven surrogate modelling approach called B-FNO, which combines BEM and Fourier neural operator (FNO) for wave analysis in varying domains and frequencies. This approach formulates wave equations as integral formulations and utilizes FNO to map problem boundaries and other parameters to boundary solutions. Compared to existing surrogate modelling techniques, the B-FNO approach offers several advantages. These include reduced problem dimensionality and computational complexity, the ability to handle exterior problems without domain truncation, and significantly improved efficiency and accuracy compared to well-known neural network surrogate models. Moreover, compared to accelerated BEM, the B-FNO approach is better behaved and requires a much smaller number of iterations. We validate the effectiveness of our method through numerical experiments on a series of 2D and 3D benchmark problems, demonstrating its potential for broad application.

Keywords Surrogate model · Acoustic wave equation · Boundary element method · Fourier neural operators

1 Introduction

Wave analysis is of critical importance in various fields and applications, including noise control, ultrasound imaging, seismic engineering, and non-destructive testing. In many cases, it becomes necessary to conduct parametric analysis, involving a series of analyses corresponding to different parameters. For instance, in the design of sound systems

and broadband noise absorbers, frequency sweep analysis is often employed to evaluate their performance across a range of frequencies. Similarly, during the design of wave-controlling metamaterials, repetitive wave analysis is conducted to evaluate the performance of the design solution as it evolves throughout the design process [1, 2].

Conducting parametric wave analysis for complex engineering problems, especially those involving unbounded and/or changing domains, can pose significant computational challenges when using conventional volume-discretization based numerical methods like the finite element method (FEM). The high computational cost associated with FEM renders it impractical for such parametric analyses. In contrast, the boundary element method (BEM) offers a lower-dimensional problem by discretizing only the domain's boundary. BEM is especially suitable for problems with unbounded domains, such as those

✉ Wenjing Ye
mewye@ust.hk

1 Department of Mechanical and Aerospace Engineering, The Hong Kong University of Science and Technology, Hong Kong SAR, P. R. China

2 Department of Mechanics and Aerospace Engineering, Southern University of Science and Technology, Shenzhen, P. R. China

encountered in metamaterial design. However, the fully populated system matrix in conventional BEM can still lead to computational challenges. Although accelerated techniques like fast multipole BEM [3–5], adaptive cross approximation BEM [6], and pre-corrected fast Fourier transform BEM [7] have reduced the computational cost to $O(NlogN)$, where N is the system size, conducting large-scale wave analysis across different problem settings using BEM remains resource-intensive. This is particularly true for large-scale problems with high wave frequencies due to the poor condition of their system matrices. Finding a good pre-conditioner to reduce the number of iterations is still an on-going effort [8].

Various surrogate/reduced order modeling techniques have been developed to reduce the computational cost of parametric wave analysis. These techniques range from conventional projection-based reduced order modelling to more recent machine learning-based surrogate models. In [9, 10], project-based model order reduction (MOR) methods were developed for conventional BEM systems, aiming to reduce the computational cost of multi-frequency acoustic wave analysis. A key step in this approach is to construct a series of frequency-independent matrices by expanding frequency-dependent BEM kernels, which is non-trivial especially for problems with complex boundary conditions [11]. To overcome this challenge, a matrix-free MOR method was proposed [11]. This method operates on the transfer functions between system inputs and outputs, circumventing complications arising from complex boundary conditions and enabling integration with existing acceleration techniques. Nevertheless, these conventional projection-based reduced order modelling methods were primarily developed for problems with fixed domains, extending them to solve design problems involving continuously changing domains is challenging.

Recently, there has been a growing utilization of machine learning models based on artificial neural networks in wave analysis and metamaterial design. Examples include, but are not limited to, the use of Gaussian radial basis function networks for predicting wave band amplitude [12], convolutional neural networks (CNN) for forecasting acoustic wave absorption spectra across different absorber structures [13], as well as predicting spatial loudness distribution for various scatterers [14]. Furthermore, multi-scale convolutional neural networks have been employed to predict the propagation of acoustic waves [15]. Generative adversarial networks (GAN) have also found application in designing meta-porous materials for sound absorption [16], as well as metamaterials with specific transmission characteristics [17] and reduced total scattering cross-section [18]. However, these end-to-end models are problem-specific, and their applicability has predominantly been limited to relatively simple 2D problems due to the requirement for extensive training data. Moreover,

their performance is highly dependent on the mesh resolution, necessitating retraining for different resolutions.

In an effort to minimize the reliance on training data and achieve mesh independence, several physics-informed neural network models have been developed to solve partial differential equations (PDE) [19–21]. These network models map the location of a point inside the domain to its solution for a given problem. The training of the network is guided by the underlying PDE or the associated energy formulation and boundary conditions. As such, no or very little training data are needed. Recently, these methods have been extended to solve boundary integral equations [22]. However, these models tend to be much more difficult to train and require lengthier training processes than for purely data-driven approaches. Additionally, they are designed to solve one specific problem with fixed parameters. For a new set of parameters, e.g., a different structure or different boundary conditions, a new ANN model must be constructed and re-trained.

Recently a new type of artificial neural network modes entitled as Neural Operators have emerged as powerful network models that map between two infinite-dimensional function spaces. Unlike physics informed ANNs, neural operators are solution operators, i.e., they can output solutions corresponding to different parametric settings without re-training. Additionally, these operators are resolution invariant. A model trained using a coarse mesh can be directly used to obtain solutions on fine meshes. Various neural operators have been proposed [23–28]. Among them, the Fourier neural operator (FNO) has emerged as a promising approach to approximate complex operators arising in PDEs because of its state-of-the-art approximation capabilities [26]. This method has been applied successfully to solve various PDEs. It has been employed to compute the solutions of the Navier-Stokes equation with different initial conditions in the turbulent regime, outperforming several well-known representative ANN models [26]. For wave analysis, a recent work applied the method to perform elastic wave analysis in a finite 3D heterogenous medium characterised by different shear velocities [28]. To reduce the computational burden which increases with the number of dimensions, factorized F-FNO [29] method was employed to reduce the number of convolutional kernel weights. Although the number of weights is reduced, the computational cost of F-FNO is not necessarily less than that of the original FNO as shown in [29]. This is because the Fourier transfer and its inverse transfer contribute a significant portion of the computational cost. Even with the fast Fourier transfer technique, the computational complexity is still $O(NlogN)$, where N is the total number of grid points inside the domain, which grows linearly with the dimension. Another study leveraging the FNO was conducted to comprehend frequency domain 2D finite seismic wavefields in the context of varying velocity models for seismic imaging [30]. Their proposal of

a parallel FNO (PFNO) framework for different frequencies, demonstrated high accuracy even in the presence of data noise [30]. Combining FNO with DeepOnet has also been proposed and applied to perform full waveform inversion in a 2D rectangular domain [31]. All applications demonstrated so far are for solving PDEs in finite domains. It is not straightforward to effectively extend the method to solving exterior problems due to the challenge posed by the infinite domain. In addition, the efficiency of the FNO should be further improved for dealing with 3D problems.

In this work, we propose a data-driven surrogate modelling approach entitled as B-FNO based on the BEM and the FNO, targeting at wave analysis of problems with changing domains and frequencies. We first cast wave equations into their integral formulations. We then construct Fourier neural operators to map the boundaries of problem domains and other parameters to the boundary solutions. Once all the boundary quantities are obtained, the wave quantities at any points inside the domain, whether it is finite or infinite, can be calculated via an integral formulation. The advantages of the proposed method are that (1) it reduces the dimension of the problem by one and thus reduces the size of the problem and the computational complexity of the Fourier neural operator, (2) it can deal with exterior problems without the need to discretize the infinite domain or artificially truncate the domain, and (3) it is more efficient and accurate than some well-known representative ANN models.

This paper is organized as follows. In Sect. 2, the BIE formulation for the acoustic wave equation and the basic framework of the FNO are introduced. The detailed B-FNO method is then described. In Sect. 3, numerical experiments on a series 2D and 3D benchmark problems are described and results are presented. Ablation study and comparison with BEM and other neural network models are presented and discussed. The conclusion and future work are described in Sect. 4.

2 Methods

2.1 Boundary integral formulation of acoustic wave equation

The type of problem we focus in this work is acoustic wave analysis; however, the method proposed is also applicable to elastic and electromagnetic wave analyses. The linear acoustic equation in the frequency domain is governed by the Helmholtz equation:

$$\nabla^2 \varphi + k^2 \varphi + Q\delta\left(\mathbf{x}, \mathbf{x}_Q\right) = 0, \quad \forall x \in D \tag{1}$$

where φ is the complex acoustic pressure at location $\mathbf{x}$, k is the wavenumber, and $Q\delta\left(\mathbf{x}, \mathbf{x}_Q\right)$ represents a point sound source at point $\mathbf{x}_Q$ inside domain D, with amplitude of Q.

There are three types of boundary conditions typically prescribed on the boundary S of domain D: (1) sound pressure is given by $\varphi = \overline{\varphi}$; (2) particle velocity is given by $q \equiv \frac{\partial \varphi}{\partial n} = \overline{q} = i\omega \rho v_n$; and (3) the impedance is given by $\varphi = Z v_n$, where the overbar symbol indicates a given value, ρ is the density of acoustic medium, v_n is the normal velocity of the acoustic medium, and Z is the specific acoustic impedance. For exterior problem, besides abiding the boundary conditions, the field at infinity should comply with the subsequent Sommerfeld radiation condition:

$$\lim_{R \to \infty} \left[R \left| \frac{\partial \varphi}{\partial R} - ik\varphi \right| \right] = 0$$

where R denotes the radius of an encompassing sphere around the structure and φ designates the radiated wave in a radiation issue or the scattered wave during a scattering predicament.

Applying the Green's second identity and the property of Dirac function, Eq. (1) can be formulated into a boundary integral equation, termed as the conventional boundary integral equation (CBIE):

$$c(\mathbf{x})\varphi(\mathbf{x}) = \int_S \left[G(\mathbf{x}, \mathbf{y}, \omega)q(\mathbf{y}) - F(\mathbf{x}, \mathbf{y}, \omega)\varphi(\mathbf{y}) \right] dS(\mathbf{y}) + \varphi^I(\mathbf{x}) + QG(\mathbf{x}, \mathbf{x}_Q, \omega) \tag{2}$$

$$G(\mathbf{x}, \mathbf{y}, \omega) = \begin{cases} \frac{i}{4} H_0^{(1)}(kr), & \text{for two dimensions} \\ \frac{1}{4\pi r} e^{ikr}, & \text{for three dimensions} \end{cases}$$

$$F(\mathbf{x}, \mathbf{y}, \omega) = \begin{cases} -\frac{ik}{4} H_1^{(1)}(kr)r_{,j}n_j(y), & \text{for two dimensions} \\ \frac{1}{4\pi r^2}(ikr - 1)r_{,j}n_j(y)e^{ikr}, & \text{for three dimensions} \end{cases}$$

where $\varphi^I(\mathbf{x})$ represents the incident wave, which is absent in radiation problems, r is the distance between a source point $\mathbf{x}$ to a field point $\mathbf{y}$, and the $H_1^{(1)}(kr)$ denotes the Hankel function of the first kind. Kernel G, also recognized as the 'fundamental solution' or 'Green's Function', outlines the response at a certain field point due to a solitary source at a source point. Kernel F is its normal derivative. The CBIE essentially performs a convolution of kernels G and F along the boundary. $c(\mathbf{x})$ is a coefficient with its value depends on the location of $\mathbf{x}$:

$$c(\mathbf{x}) = \begin{cases} 1, \forall \mathbf{x} \in D; \\ \frac{1}{2}, \forall \mathbf{x} \in S \text{ (smooth)}; \end{cases}$$

With the given boundary conditions, Eq. (2) with $c(\mathbf{x}) = 1/2$ is first solved for unknown boundary quantities. The pressure inside the domain is then found by computing the integral in Eq. (2) with $c(\mathbf{x}) = 1$ and the known boundary values.

One critical issue of CBIE for exterior acoustic problems is the non-uniqueness at fictitious frequencies, which are related to the eigenfrequencies of the corresponding interior

acoustic problems. A dual formulation consisting of the CBIE and its normal derivative was proposed by Burton and Miller to resolve this issue [32]. Taking the derivate of the CBIE with respected to the normal direction at the source point x, hypersingular BIE (HBIE) is obtained. Then, the Burton-Miller (B-M) formulation can be written symbolically as:

$$CBIE + \beta \ HBIE = 0$$

where β is a coupling coefficient. In this paper, $\beta = -ih$ is used, with h being the typical element size in the BEM mesh.

Equation (2) is solved by discretizing the boundary of the domain D. The resulting discretized linear system can be typically solved by the generalized minimum residual method (GMERS) [33] in which the solution is found in the Krylov space formed by a span of $\{x_0, x_1 = Ax_0, \ x_2 = Ax_1, \ \cdots, x_n = Ax_{n-1}, \ \cdots\}$ where x_0 is the discretized initial guess of the solution and x_n is the solution at the n-th iteration. $\mathbf{A}$ is the system matrix with its components being the integrals of kernels evaluated at each element.

2.2 Basic framework of the original FNO

The original FNO is a neural operator that maps a parameter space to the corresponding solution space in a finite domain. The key idea of the FNO is to add a non-local integral operation to the usual network updating procedure in each hidden layer, as shown in Eq. (3).

$$v_{t+1}(x) := \sigma\left(Wv_t(x) + \left(\mathcal{K}(a;\varphi\,)v_t\right)(x)\right), \ \forall\, x \in D \qquad (3)$$

where v_t is the high-dimensional representation of the solution at the t-th hidden layer, W and σ stand for a linear transformation and non-linear activation function, a represents the problem parameters, φ denotes the network parameters and $\left(\mathcal{K}(a;\varphi\,)v_t\right)(x)$ is the non-local integral defined as $\left(K(a;\varphi\,)v_t\,\right)(x) = \int_D \kappa_\varphi\,(x-y,a)v_t(y)\mathrm{d}y$. The convolutional nature of the integral allows it to be computed via fast Fourier Transform (FFT):

$$\left(K(a;\varphi\,)v_t\,\right)(x) = \mathcal{F}^{-1}(\mathcal{F}(\kappa_\varphi\,) \cdot \mathcal{F}(v_t))(x) = \mathcal{F}^{-1}(R_\varphi \cdot (\mathcal{F}v_t))(x)$$

where $\mathcal{F}$ denotes the Fourier transform of a function and $\mathcal{F}^{-1}$ is its inverse. R_φ is a tensor containing the Fourier coefficients of the kernel function κ_φ, which is determined through learning via network updates. During the computation, high-order modes are filtered out, resulting in model speed-up. Additionally, this filtration aids in removing high-frequency noises present in the feature information.

2.3 B-FNO

The B-FNO predicts boundary solutions for a range of problems characterized by different parameters. In this study, we focus on wave scattering scenarios involving various structures. Therefore, the parameter space considered encompasses both the varying structures and incident wave frequencies. We define the geometry of these structures using a set of boundary nodes extracted from a boundary mesh. To input the wave frequency, multiple approaches can be used. One straightforward approach is to directly input the wave number as an additional channel. However, the performance of B-FNO using this approach is less satisfactory. Through a thorough investigation, it has been discovered that the most accurate results are achieved by implicitly representing the frequency using the boundary pressure field corresponding to the incident wave. Figure 1 shows the architecture of the B-FNO network model. The inputs of the network are vectors containing the Cartesian coordinates of boundary points $x \in S$ and the incident plane wave pressure on this set of boundary points $\varphi^I(x) = e^{ik\bullet x}$, where k is the angular wave vector. The output of the network is the solution for boundary unknowns. In this work, we focus on problems involving wave scattering over hard structures. Hence the output is the sound pressure on the domain boundary $\varphi(x), x \in S$. After the boundary unknowns are solved, Eq. (2) is employed to calculate the wave field at any point inside the domain, that is $\varphi(x), x \in D$.

It is important to note that the boundary points extracted from a boundary mesh are typically unevenly distributed. To facilitate efficient FFT calculations, the inputs are transformed into a high-dimensional representation, denoted as $v_0(x) \in \mathbb{R}^{d_v}$, which is evaluated on a uniform distributed grid using a fully connected neural network called FC1. The dimension of this representation is d_v. As depicted in Fig. 1, for 2D problems, the high-dimensional representation consists d_v 1-D vectors, each with a size of N, where N is the total number of boundary points. For 3D problems, the high-dimensional representation consists d_v 2-D arrays, with each array having a size of $N_1 \times N_2 = N$, where N is the total number of boundary points.

The updating process of the high-dimensional representation, $v_t(x)$, at each Fourier layer FL follows the similar approach to the original FNO as described in Eq. (3). However, there is a distinction in that the non-local integral, $\int_S \kappa_\varphi\,(x-y,a)v_t(y)\mathrm{d}y$, is defined on the boundary instead of the entire domain. This integral bears resemblance to the boundary integrals present in the integral formulation shown in Eq. (2). The key distinction is that in Eq. (2), the kernel functions are based on the fundamental solutions of the Helmholtz's equation, whereas in B-FNO, the kernel function is treated as network parameters and is determined through minimizing the loss function of the network. There
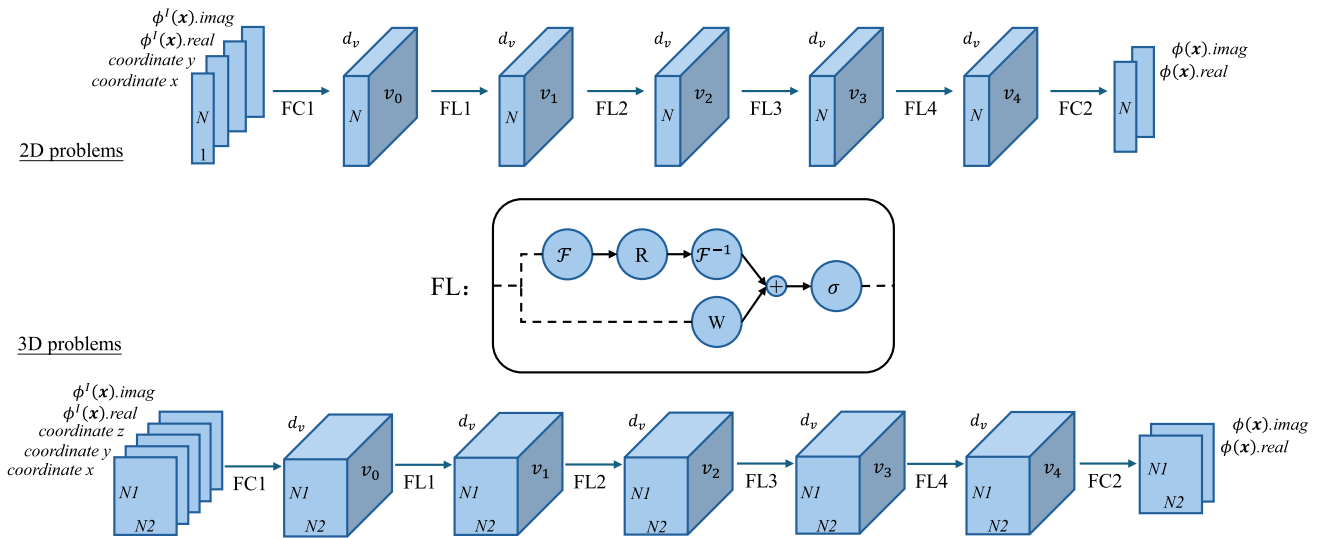
Fig. 1 Schematic of B-FNO architecture

is a certain advantage of using this data-driven approach to determine the kernel function instead of using the fundamental solutions directly as the kernel function. Firstly, no regularization is required to handle singular and/or hyper-singular integrals. The data-driven approach learns the "regularized" kernels directly. Secondly, the system exhibits better behaviour. As shown in Sect. 5, the number of Fourier layers required to achieve accurate solutions is typically much less than the number of iterations needed in GMRES, particularly for problems with ill-conditioned system matrices. Moreover, it appears to be frequency independent regardless of the condition of the system.

The updating process can be described in detail as follows. First, the FFT is employed to compute the Fourier coefficients of $v_t(\boldsymbol{x})$. Subsequently, the high-order modes are filtered out, and the remaining coefficients are multiplied with the kernel coefficient tensor $\boldsymbol{R}$. Inverse FFT is then performed on the product to obtain the updated $v_t(\boldsymbol{x})$, denoted as $v_{t+1}(\boldsymbol{x})$. Finally, after the final Fourier layer, the high-dimensional representation is projected through another fully connected neural network, FC2, to obtain the boundary solution $\varphi(\boldsymbol{x})$, for $\boldsymbol{x} \in S$.

3 Numerical experiments

A series of two-dimensional and three-dimensional scattering problems are used to examine the effectiveness of the proposed B-FNO approach. In most of these problems, a unit-amplitude plane wave with frequency ω is incident upon a collection of rigid scatterers. Additionally, a problem with a point sound source of unit amplitude is studied to assess the performance of the method with different sound

sources. Hard-wall boundary condition is imposed in all the problems.

In all the examples studied in this work, the ground truth data is generated using the conventional BEM. Constant element discretization is employed in all the problems. For three-dimensional problems, triangular constant elements are used.

3.1 2D scattering problem–elliptical scatterer

A hard-wall ellipse is subjected to a plane incident wave with a unit amplitude propagating along the positive x-direction. The geometry and associated parameters are illustrated in Fig. 2, where "a" represents the semi-major axis of the ellipse, and "b" represents the semi-minor axis. In this physical scenario, we explore two types of problems: the frequency sweeping problem with a fixed structure, and the emulation of various structures at a fixed frequency. We first assess the prediction accuracy of B-FNO for both of these
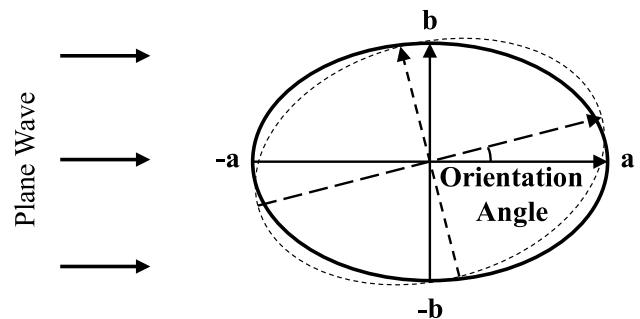

Fig. 2 Schematic of an ellipse subject to a plane wave with unit amplitude

problem types. Subsequently, we conduct an ablation study to analyse the influence of different hyperparameters on the model's performance. The hyperparameters under consideration include input forms, the dimension of the representation d_v, the number of Fourier layers, and the number of Fourier modes.

3.1.1 Prediction accuracy

The prediction accuracy is assessed by two types of error measures: the Root Mean Squared Error (RMSE) and the relative Root Mean Squared Error (rRMSE), which are defined as follows:

$$RMSE = \sqrt{\frac{1}{N} \sum_{i=1}^{N} (P_{truth,\,i} - P_{prediction,\,i})^2}$$

$$rRMSE = \sqrt{\frac{1}{N} \sum_{i=1}^{N} \frac{(P_{truth,\,i} - P_{prediction,\,i})^2}{P_{truth,\,i}^2}}$$

where P_{truth} denotes the ground truth of pressure on the boundary calculated by the conventional BEM, $P_{prediction}$ is the boundary pressure predicted by the B-FNO and N is the total number of boundary points in each sample. The rRMSE allows for a more intuitive comprehension of the error in the form of a percentage, while the RMSE gives a better reflection of accuracy when the denominator is relatively small. All errors are presented in the following format:

$$RMSE \text{ or } rRMSE = error_{mean} \pm error_{std}$$

where $error_{mean}$ and $error_{std}$ represent the average value and the standard deviation of all testing samples respectively.

In the frequency sweeping problem, the values of a and b are held constant. The orientation angle of the ellipse is set to 0, and the frequency ranges considered are presented in Table 1. In the structural change problem, the frequency remains fixed, while the ranges for a and b are also specified

in Table 1. The orientation of the ellipse is uniformly distributed within the range of 0 to π. All the results reported in Table 1 are obtained using a 4-layer FNO with $d_v = 16$ and full modes. The training samples are uniformly selected from the entire parameter range, while the testing samples are randomly chosen from the complete set of samples excluding those used for training. The Adam optimizer is employed with a learning rate of 8×10^{-4}, and the H1 norm loss is utilized as the loss function, f, which is defined as the difference between the prediction and the ground-truth.

$$\| f \|_{H1} = \left(\| f \|_{L2}^2 + \| \nabla f \|_{L2}^2 \right)^{1/2}$$

Based on the errors presented in Table 1, it is evident that B-FNO demonstrates outstanding performance in both problem types. In the frequency sweeping problem, B-FNO demonstrates its capability to handle wide frequency ranges. Although there is a slight increase in error as the frequency range expands, such as from [1, 1000 Hz] to [1, 2000 Hz], this trend is expected because the same training data and network architecture are employed in all cases. As the range broadens, the problem complexity naturally increases, which in turn requires additional training data and/or a more complex architecture to attain the same level of accuracy. The geometric variation problem follows a similar pattern. When enlarging the geometric size range, for instance, by changing the semi-major axis range from $0.6 \sim 2.7$ to $2.4 \sim 10.8$ and the semi-minor axis range from $0.4 \sim 2.3$ to $1.6 \sim 9.2$, there is a slight decrease in accuracy. However, this decrease in accuracy is minimal, indicating that the frequency level, as measured by the dimensionless wavenumber, has minimal impact on the overall accuracy.

To gain a better understanding about the performance of the method, Fig. 3 presents some additional results. Taking the model trained with ka range from 5 to 25 as an example, the training loss curve is plotted in Fig. 3(a) for 1000 epochs. It is evident that the convergence is rapid and the error could be further decreased if additional epochs are

Table 1 The performance of B-FNO in both frequency sweeping problem and structural change problem with varying dimensionless wavenumber

	Frequency sweeping problem			Structural change problem		
Dimensionless wavenumber	$0.037 \sim 37$	$37 \sim 73$	$0.037 \sim 73$	$5 \sim 25$	$30 \sim 50$	$20 \sim 100$
Semi-major axis a (m)	1.2			$0.6 \sim 2.7$	$3.6 \sim 5.4$	$2.4 \sim 10.8$
Semi-minor axis b (m)	0.8			$0.4 \sim 2.3$	$2.4 \sim 4.6$	$1.6 \sim 9.2$
Frequency (Hz)	$1 \sim 1000$	$1000 \sim 2000$	$1 \sim 2000$	272.95		
Number of samples	Training: 500, Testing: 500			Training: 1000, Testing: 400		
Number of epochs	1000			1000		
RMSE	2.02E-3± 7.65E-4	2.12E-3± 5.45E-4	3.93E-3± 1.86E-3	1.58E-3± 3.79E-4	2.02E-3± 4.66E-4	6.02E-3± 5.69E-3
rRMSE	0.011%± 0.004%	0.008%± 0.002%	0.015%± 0.006%	0.009%± 0.002%	0.008%± 0.002%	0.022%± 0.021%
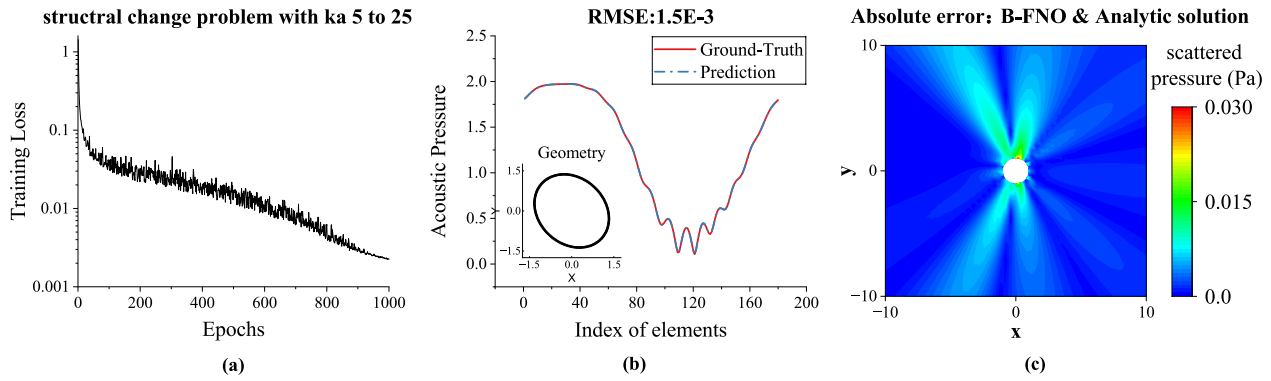
Fig. 3 **a** The loss curve for structural change problem with *ka* from 5 to 25; **b** The comparison between the boundary pressure calculated by BEM & B-FNO; **c** Absolute error of the wave field outside a circular scatterer calculated by B-FNO

used. Figure 3(b) showcases the comparison between the acoustic pressure on the boundary of an ellipse predicted by B-FNO and the ground truth, demonstrating the close alignment between the B-FNO prediction and the truth, as indicated by the precision values in Table 1. Using B-FNO, we also predict the BEM boundary solution of a circle with a radius of 1 m at a frequency of 272.95 Hz. Equation (2) is then used to calculate the scattered acoustic pressure for the entire considered field. Th analytical solution for sound pressure in this case is available and used to calculate the absolute error of the prediction:

$$p_s = -p_0 \sum_{n=0}^{+\infty} \in_n i^n \frac{J_n{'}(ka)}{H_n^{(1)}{'}(ka)} H_n^{(1)}(kr) \cos n(\theta - \theta_d)$$

where $\in_0 = 1$, $\in_n = 2$ for $n > 0$. p_0 is the pressure of the incident plane wave, r, θ are the coordinates of point in the computational domain, θ_d is the polar angle of the incident wave propagation direction, which is zero in this example and $H_n^{(1)}$ denotes the first kind of n order Hankel function. It should be noted that circular scatterers are not included in the training data, but the surrogate model still provides good results, as shown in Fig. 3(c).

3.1.2 Ablation study

In this section, we study the impact of different hyperparameters on the training accuracy of B-FNO, including frequency input form, dimension of v_t, the number of Fourier layers, and Fourier modes. To facilitate a clear interpretation of the loss curves, which can often be oscillatory, we have applied a modified approach. All the loss curves presented in this section have been processed using a moving average method. Each point in the smoothed curve is generated by averaging the corresponding point and its next 49 consecutive points in the original loss curve.

We employ the ellipse with a semi-major axis of 1.2 and a semi-minor axis of 0.8, along with a frequency range from 1 to 1000 Hz, as our benchmark for the frequency sweeping problem study. On the other hand, for the structural change problem, we select the ellipse with a semi-major axis ranging from 0.6 to 2.7 and a semi-minor axis ranging from 0.4 to 2.3 at a frequency of 272.96 Hz as the benchmark.

In all figures presented in the subsequent sections, the top figures display the complete training loss curve, and a logarithmic scale is used to label the training loss value. The bottom figures provide zoomed-in views of specific areas of interest from the top figures. In the zoomed-in figures, a linear scale is employed to represent the training loss. The average testing relative errors (rRMSE) of different cases are listed in the tables next to the top figures.

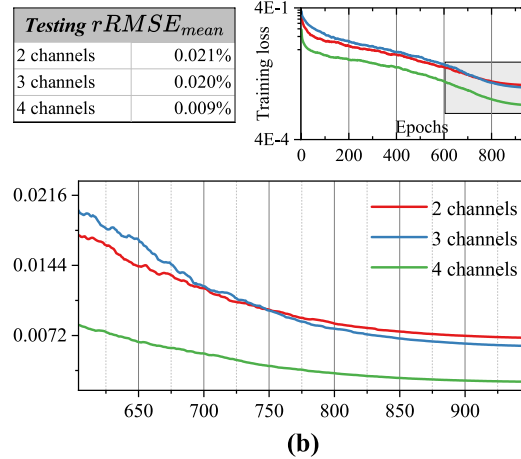3.1.2.1 **Comparison of different frequency input forms** While the geometry of the structure can be prescribed relatively straightforward by using the nodes from a boundary mesh, incorporating the wave frequency into the network poses a more challenging task. A simplistic approach is to input the wavenumber as an additional input channel. Hence, in the frequency sweeping problem, a total of three input channels (coordinates x, coordinates y, wavenumber k) are utilized. However, the accuracy of this approach is unsatisfactory, as indicated by the loss curve in Fig. 4(a). Through extensive experimentation, we have found that using the incident wave pressure at the boundary to implicitly represent the frequency yields the best accuracy. In this approach, four input channels are used: coordinates x, coordinates y, real part of plane wave pressure, and imaginary part of plane wave pressure. The training loss achieved with these four channels is significantly lower than that attained with the three channels as depicted in Fig. 4(a).

For the structural change problems, where the frequency is fixed, it may seem unnecessary to include the frequency as an input. Two input channels corresponding to the x and y coordinates of the boundary nodes should

Different input forms in frequency sweeping problem

Testing $rRMSE_{mean}$	
3 channels	0.015%
4 channels	0.001%
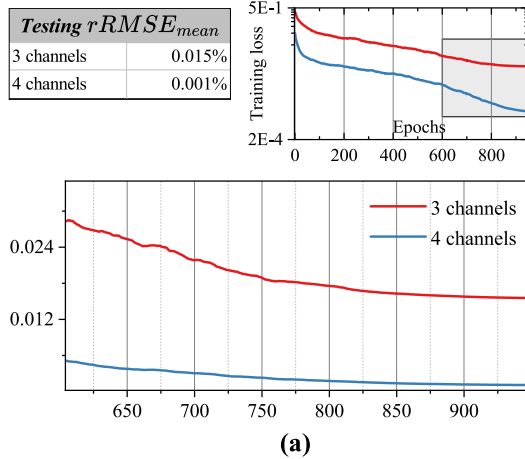
Different input forms in structural change problem

Testing $rRMSE_{mean}$	
2 channels	0.021%
3 channels	0.020%
4 channels	0.009%

(a) **(b)**

Fig. 4 Training loss curves corresponding to cases with different input forms in **a** frequency sweeping problem and **b** structural change problem. The bottom figures are the zoomed-in views of the shaded areas in the top figures

theoretically be sufficient. However, it has been discovered that by including the frequency input in the same format as the four channels, the training loss further decreases, resulting in significantly lower training loss, as illustrated in Fig. 4(b).

Interestingly, for both cases, employing four input channels, which incorporate the plane wave sound pressure acting on the boundary, yields higher accuracy. While the plane wave pressure can be seen as indicative of the wave frequency, this input format captures the oscillatory physical nature of the sound wave at different frequencies. Consequently, it facilitates faster and more effective learning for the network model. This input form has also proven

beneficial in achieving good accuracy in the subsequent example involving a point sound source.

3.1.2.2 **Effect of the dimension of v_t** In B-FNO, the input first passes through a lift layer P, which elevates the original input to a higher dimensional representation v through a shallow fully connected neural network. Theoretically, lifting to a higher-dimensional space can encapsulate more information and consequently yield superior precision in subsequent learning. However, a trade-off evidently exists between accuracy and time cost. As Fig. 5 illustrates, once the number of latent channels, d_v, reaches 64, increasing the dimensionality results in a smaller loss reduction than before and notably requires significantly more

Different number of latent channels in frequency sweeping problem

Testing $rRMSE_{mean}$	
32 channels	0.018%
64 channels	0.011%
128 channels	0.008%
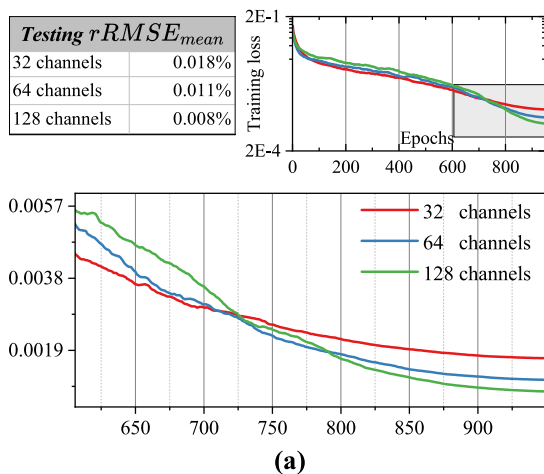
Different number of latent channels in structural change problem

Testing $rRMSE_{mean}$	
32 channels	0.020%
64 channels	0.010%
128 channels	0.005%

(a) **(b)**
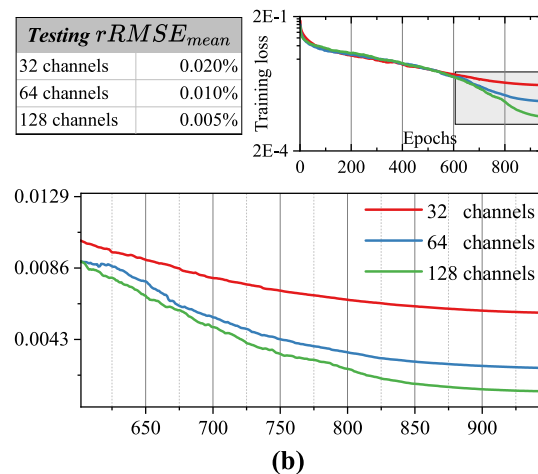
Fig. 5 Training loss curve corresponding to cases with different numbers of latent channels in **a** frequency sweeping problem and **b** structural change problem. The bottom figures are the zoomed-in views of the shaded areas in the top figures

computational time. Therefore, in this work, we typically opt for 64 latent channels.

3.1.2.3 **Effect of fourier layers** Regarding the number of Fourier layers in B-FNO, the results shown in Fig. 6 indicate that utilizing 4 layers yields significantly higher accuracy than deploying 2 layers, while the application of 8 layers does not lead to a substantial enhancement. Considering the trade-off between accuracy and efficiency and given that the use of 8 layers demands twice the computational time compared to 4 layers, 4 layers seem to be a good choice and are used in all examples considered in this work.

3.1.2.4 **Effect of fourier modes** In these specific types of problems, the sample dataset comprises 180 boundary grids, corresponding to 180 modes that constitute the full mode set. Notably, it has been observed that even utilizing only a tenth of the modes can lead to satisfactory accuracy in these cases. However, it is evident that the highest accuracy is attained when employing the full mode set, as shown in Fig. 7. During the implementation of B-FNO, the representation v_t is initially transformed using the Fast Fourier Transform (FFT), followed by discarding the high modes. Subsequently, an inverse transformation is performed. While this approach does save some computational time, the time saved is not significant. Furthermore, when conducting
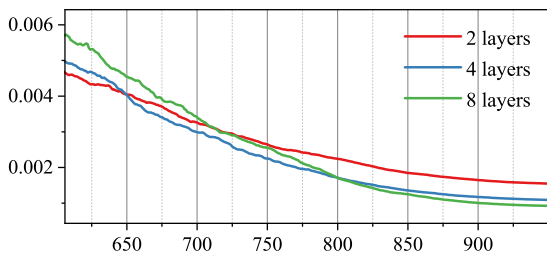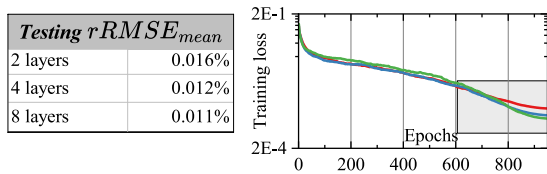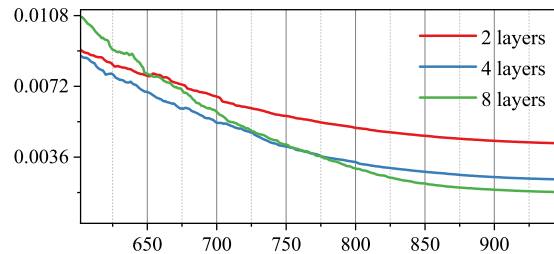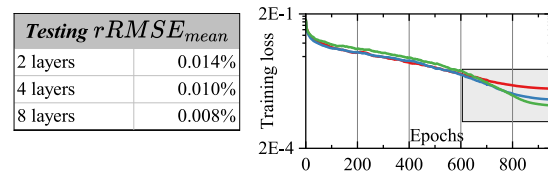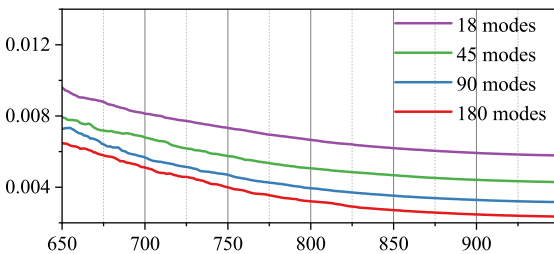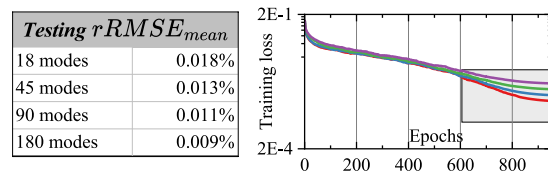

Fig. 6 Training loss curves corresponding to cases with different numbers of Fourier layers in **a** frequency sweeping problem and **b** structural change problem. The bottom figures are the zoomed-in views of the shaded areas in the top figures
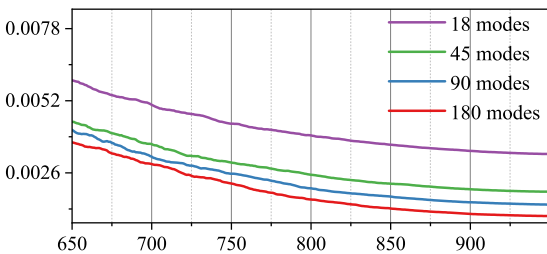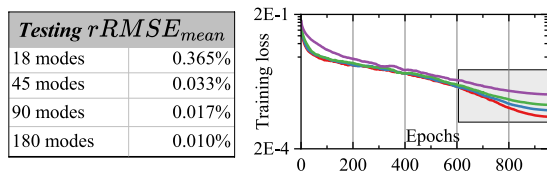
Fig. 7 Training loss curves corresponding to cases with different numbers of Fourier modes in **a** frequency sweeping problem and **b** structural change problem. The bottom figures are the zoomed-in views of the shaded areas in the top figures

training for more complex models in subsequent examples, the accuracy advantage of utilizing the full modes becomes more apparent. Hence, we choose to sacrifice a little time in exchange for higher precision in the remaining examples.

## 3.2 2D scattering problem–Helmholtz resonator (HR)

A Helmholtz resonator is a widely utilized structure in the field of sound engineering. It comprises two main components: a cavity and a neck. The cavity is connected to the outside through the neck, much like a bottle with its neck as the opening. When external forces, such as airflow, disturb the air in the neck of the resonator, it oscillates and causes the air within the cavity to resonate. At the point of resonance, the sound intensity surrounding the resonator experiences a notable reduction. Therefore, one common application of HRs is in sound energy absorption.

The key design variables of a HR are its cavity and neck dimensions, as the resonant frequency of a HR is predominantly influenced by these factors. Thus, in this particular example, we will conduct simulations of wave scattering over HRs with varying dimensions of the neck and cavity, covering a range of frequencies. Unlike the previous example, where only the frequency or structure varies, in this case, we will assess the performance of the B-FNO on problems with varied structure and frequency.

The geometry and relevant parameters of the HR are depicted in Fig. 8, with "w1" and "h1" representing the width and height of the neck, while "w2" and "h2" denote the width and height of the cavity, respectively. In this example, we fix "w2" and "h2" and only vary "w1" and "h1" to reduce the training time. The ranges for the two geometrical parameters are listed in Table 2. The frequency range considered is [500 Hz, 1500 Hz], and the corresponding dimensionless wavenumber range is [5, 20]. Similar to the previous example, the B-FNO maps the positions of boundary nodes and the frequency in the form of incident plane wave pressure to the corresponding boundary solution.

A total of 25,600 h are generated and wave analysis is performed on each of them using the conventional BEM. Among the 25,600 boundary solutions, 10,000 of them are used for training and the 5000 of the rest is randomly selected for testing. The training samples are drawn uniformly within the entire ranges of geometric parameters. For frequency sampling, a non-uniform sampling strategy is employed. Due to the resonance characteristics of HRs, the

Fig. 8 Schematic of Helmholtz resonator
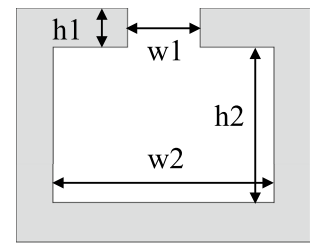
sound pressure varies more rapidly on the boundary near resonance and exhibits different characteristics than off-resonance pressures. To capture the complex relationship, more frequency samples should be drawn near the resonant frequencies. By examining the pressure peak of each HR within the frequency range, resonant frequencies of each HR are estimated. Then, 8 sampling points are densely arranged around each resonant frequency, followed by a uniform distribution of sampling points within the remaining frequency range.
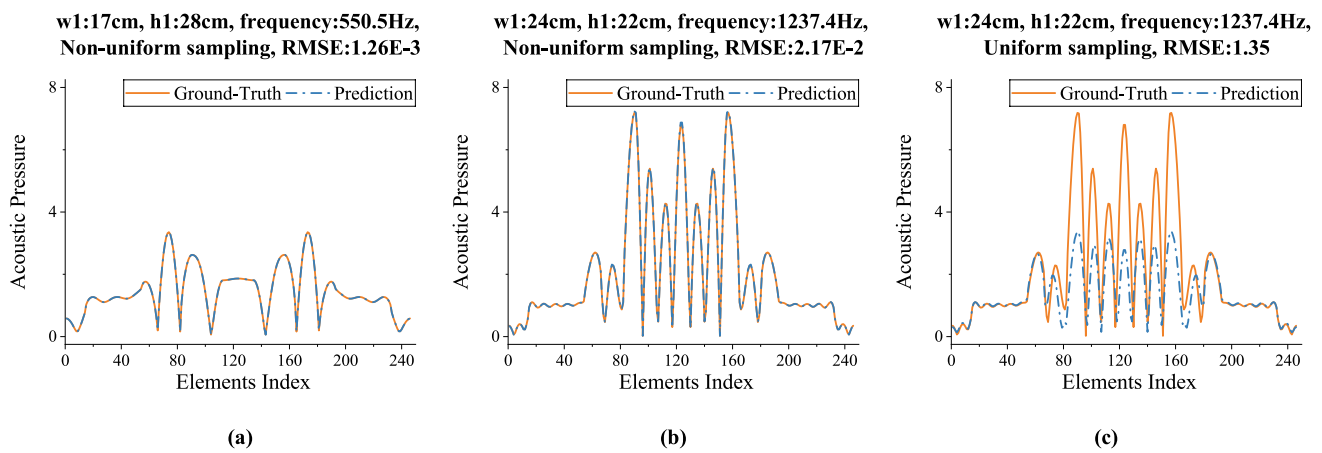
The mean and standard deviations of the RMSE and rRMSE for 5000 testing samples are provided in Table 2. The combination of 10,000 training data and the non-uniform sampling strategy has resulted in excellent overall accuracy. However, it is worth noting that the standard deviation of RMSE is relatively high, likely due to the presence of larger errors in resonant HRs. Figure 9 illustrates the pressure solutions obtained using B-FNO and conventional BEM for two representative HR cases. The results shown in Fig. 9(b) and (c) correspond to a resonant HR, while the result in Fig. 9(a) pertains to a non-resonant HR. Upon comparing these results, it is evident that the prediction accuracy is higher for non-resonant HRs compared to resonant HRs. However, when examining the solutions obtained with and without utilizing the non-uniform sampling strategy, as depicted in Fig. 9(b) and (c), a significant improvement is observed in Fig. 9(b), highlighting the effectiveness of this sampling strategy. It is anticipated that incorporating more training data near resonance will further enhance the accuracy of the predictions.

## 3.3 3D scattering problem–multiple Helmholtz resonators

In this section, we delve into a more intricate setup involving multiple Helmholtz resonators. Our configurations encompass four resonators of the same size arranged linearly as shown in Fig. 10(b) and four resonators of varying

Table 2 The parameter ranges of 2D HRs and the prediction accuracy of B-FNO in 2D HR scattering problems

w1 (cm)	w2 (cm)	h1 (cm)	h2 (cm)	Sampling strategy	RMSE	rRMSE
10~25	40	15~30	40	Non-uniform	3.53E-3 ± 3.31E-3	0.01% ± 0.06%
				Uniform	3.27E-2 ± 1.9E-1	0.12% ± 0.62%

w1:17cm, h1:28cm, frequency:550.5Hz, Non-uniform sampling, RMSE:1.26E-3

w1:24cm, h1:22cm, frequency:1237.4Hz, Non-uniform sampling, RMSE:2.17E-2

w1:24cm, h1:22cm, frequency:1237.4Hz, Uniform sampling, RMSE:1.35

(a) (b) (c)

Fig. 9 Comparison between the boundary pressure calculated by BEM (ground-truth) & B-FNO: **a** a non-resonant HR, **b** HR near the resonant frequency, B-FNO using a non-uniform sampling training set, **c** HR near the resonant frequency, B-FNO using a uniform sampling training set

(a) (b) (c)
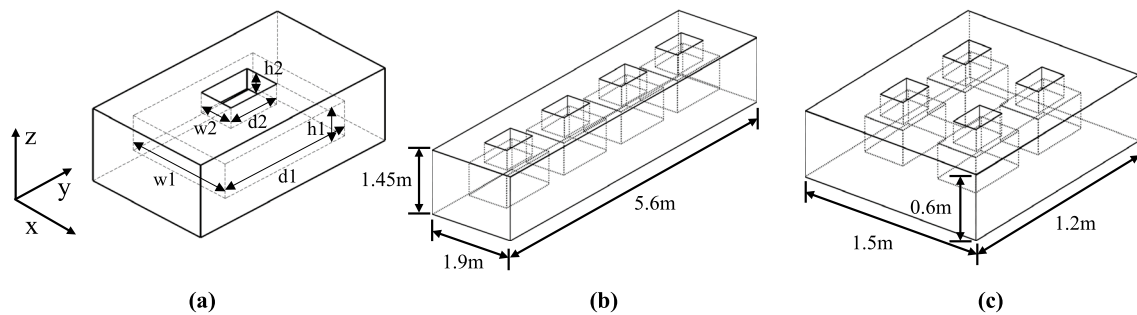
Fig. 10 **a** Schematic of 3D Helmholtz resonator and it's relative parameter. **b** linearly arranged identical resonators. **c** resonators of varying dimensions set up in a 2×2 matrix

dimensions set up in a 2×2 matrix as shown in Fig. 10(c). The linear arrangement of four identical resonators seeks to achieve a cumulative interference effect, enhancing or negating resonance at specific frequencies. It's crucial in designing systems that require modulation of frequencies, such as noise cancellation technology or signal amplification. The 2×2 matrix, consisting of resonators with varying dimensions, adds another layer of complexity to the tests. The matrix introduces a myriad of combinations, resulting in varying frequency responses and vibrational modes. Such a configuration finds its importance in offering advanced control over broadband frequencies.

The utilization of such complex geometries emphasizes the versatility and computational capabilities of B-FNO, showcasing its prowess in tackling convoluted scenarios effectively. The parameters for defining a single HR are shown in Fig. 10(a), where "w1", "d1", and "h1" represent the length, width and height of the cavity, and "w2", "d2", and "h2" denote the length, width and height of the neck, respectively.

3.3.1 HR matrix

The 2 by 2 arranged HRs of varying sizes are impinged on by an incident plane wave with a direction along the negative z axis, with a frequency of 500 Hz. The dimensions and varying window sizes of each HR are listed in Table 3. The entire structure is a rectangular structure with an external size of 1.5 m in length, 1.2 m in width, and 0.6 m in height. The structure's surface is discretized into 4,880 triangular constant elements. The coordinates of the centroids of these triangular elements, along with the incident plane wave pressure at each point, serve as inputs for the B-FNO method. These inputs are reshaped into five 2D arrays of size 61×80. Although only four HRs are considered in this example, the variations in length and width across the four HR windows lead to a rapid expansion in the number of required training data. If we were to uniformly sample only 5 points within the range of dimensions for "w2" and "d2," the dataset would already comprise nearly 400,000 samples. This clearly highlights the geometric complexity of the structure.

Table 3 The parameter ranges of 3D HR structures and the prediction accuracies of B-FNO in the corresponding scattering problems

Problems	B-FNO input	w2 (cm)	d2 (cm)	h2 (cm)	w1 (cm)	d1 (cm)	h1 (cm)	RMSE	rRMSE
2×2 varied HRs	Coordinates & plane wave pressure	25~45	15~30	20	60	45	32.5	5.29E-2± 3.26E-3	0.05%± 0.03%
4×1 identical HRs	Coordinates & plane wave pressure	50~130	30~80	50	150	100	75	1.75E-3± 1.14E-2	0.01%± 0.04%
	Coordinates & point source pressure							1.16E-3± 6.39E-3	0.009%± 0.03%

In the context of so many parameters changing at the same time, it has been found that 20,736 training samples are adequate to achieve a high accuracy, as shown in Table 3. From the testing dataset, a representative structure is randomly selected. The discretized structure, along with the boundary pressure computed using the B-FNO method, is illustrated in Fig. 11(a) and (b). For comparison purposes, the ground-truth calculated from the BEM is also depicted in Fig. 11(c). It is evident that the boundary sound pressures calculated by both methods exhibit excellent agreement. The average relative Root Mean Square Error (rRMSE) across 10,000 testing samples is 0.05%.

3.3.2 Linearly arranged HR structure

In this example, we examine a 3D scattering problem involving a point sound source. The structure consists of four identical HRs arranged linearly. A point source with a frequency of 400 Hz and a unit amplitude is incident upon this HR structure. The coordinates of the point source are (0.95, 2.8, 2). The dimensions of each HR, including the ranges of the width and length of the neck, are provided in Table 3. The external dimensions of the structure, as illustrated in Fig. 10(b), are 5.6 m x 1.9 m x 1.45 m. The surface of the structure is discretized into 16,416 triangular elements. The coordinates of the centroids and the plane wave pressure at each centroid serve as inputs for the B-FNO network. These inputs are reshaped into five 2D arrays of size 144×114.

Due to the uniformity in the dimensions of the four HRs, this example involves fewer variables, resulting in a significant reduction in the size of the training set. With only 3,000 training samples, B-FNO achieves the precision indicated in Table 3. In Fig. 12, we present the discretized structure for one testing sample, along with the boundary pressures calculated using B-FNO and the BEM. These values are shown on the reshaped spatial array. Once again, there is excellent agreement between the predictions and the ground-truth values. The average relative RMSE (rRMSE) across 1000 testing samples in this case is 0.01%.

An important aspect of this example is the utilization of a unit point source as the incident sound source. Consequently, the frequency input incorporates the pressure exerted by the point source on the surface of the structure, resulting in a high level of accuracy. Interestingly, even when using the plane wave pressure as the frequency input, a considerable degree of accuracy is maintained. Table 3 demonstrates that the accuracy achieved with the plane wave pressure input is slightly lower than that obtained with the point source. Nevertheless, when faced with more complex sound source scenarios, we believe that directly inputting the pressure exerted
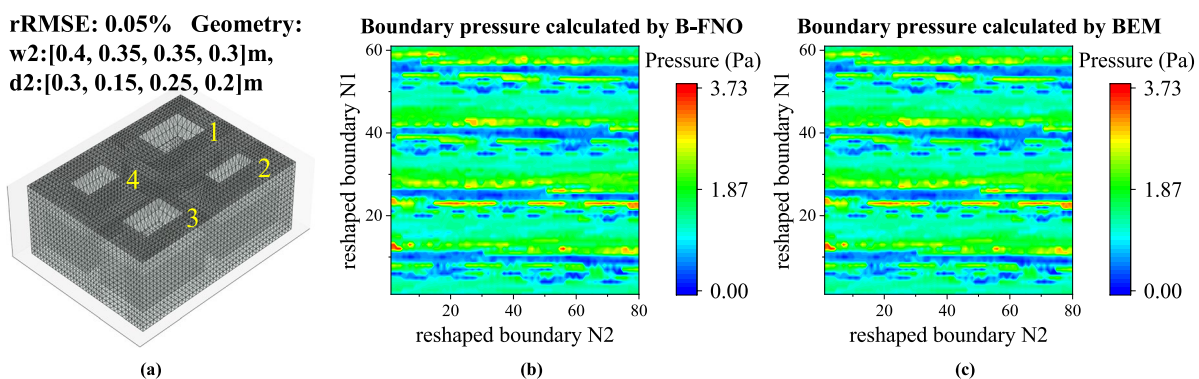
Fig. 11 **a** A discretized structure of 2 by 2 arranged HRs. The mean testing rRMSE is 0.05%. The length and the width of each neck in the four HRs are No.1 (0.4 m, 0.3 m), No. 2 (0.35 m, 0.15 m), No. 3 (0.35 m, 0.25 m) and No. 4 (0.3 m, 0.2 m) respectively. **b** The abso-lute pressure on the 2D reshaped spatial array calculated by B-FNO. **c** The absolute pressure on the 2D reshaped spatial array calculated by BEM
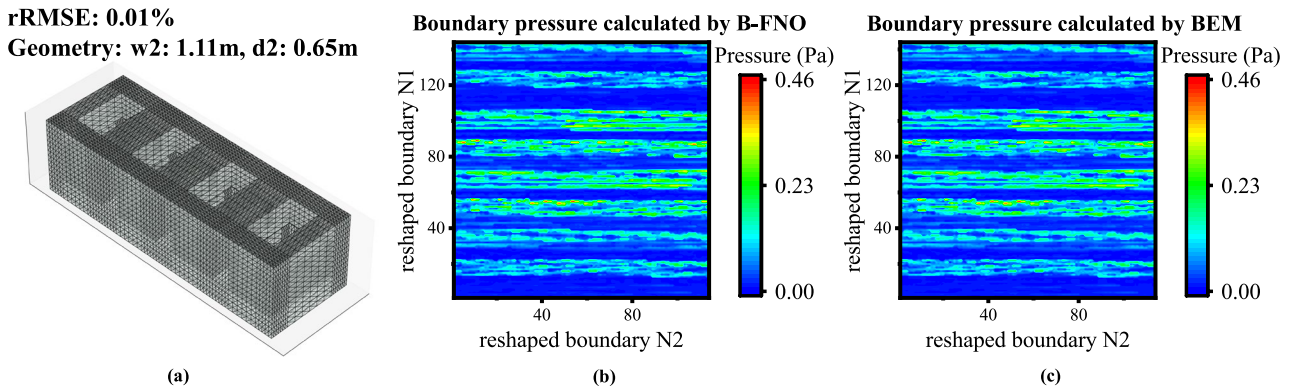
Fig. 12 **a** The discretized structure of linearly arranged identical HRs. The mean testing rRMSE is 0.01%. The length and the width of each neck are 1.11 m and s 0.65 m respectively. **b** The absolute pressure on the 2D reshaped spatial array calculated by B-FNO. **c** The absolute pressure on the 2D reshaped spatial array calculated by BEM

by the sound source on the structure's surface would better ensure the accuracy of B-FNO.
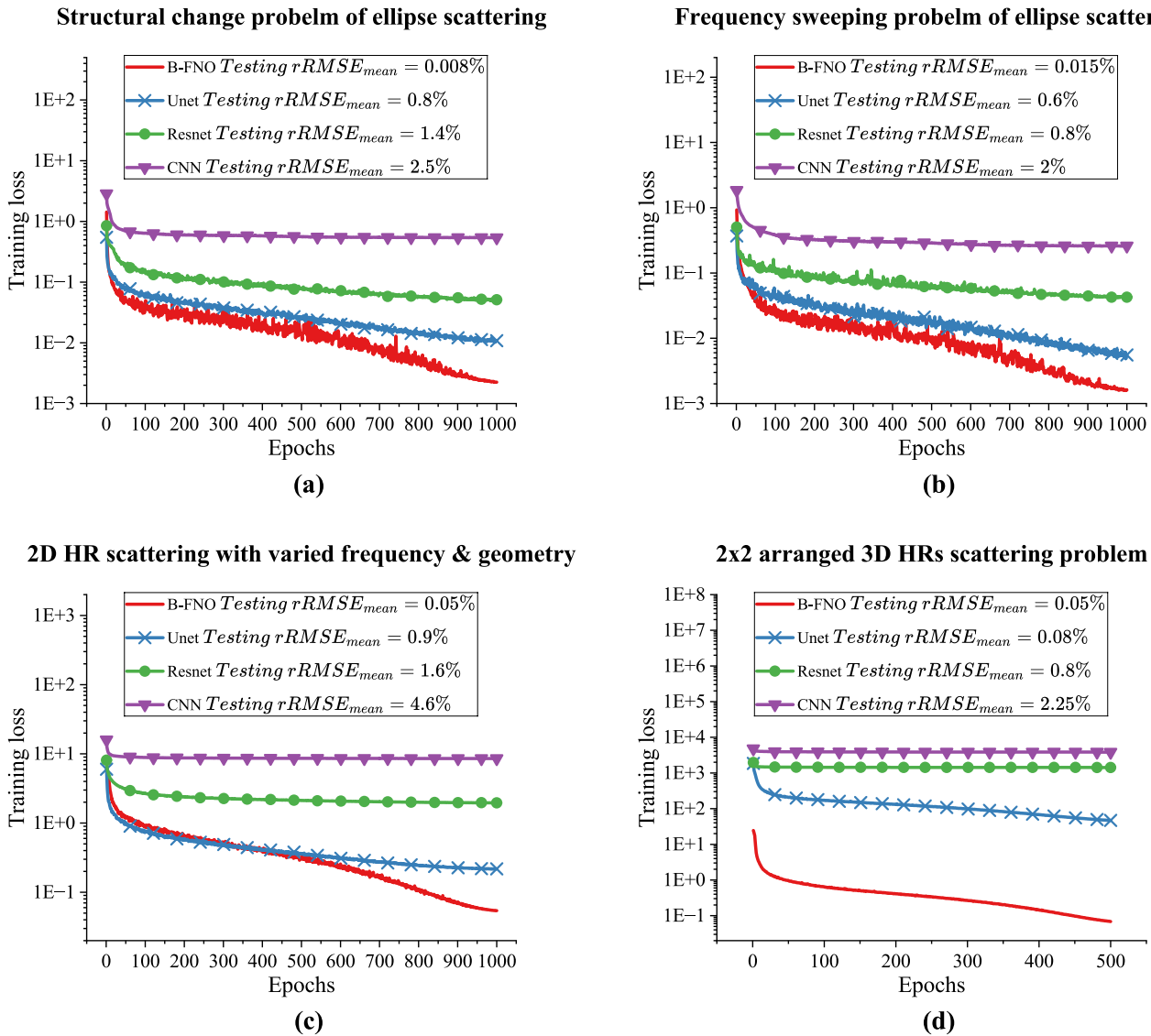
4 Comparison of B-FNO with other network structures

In this section, we compare the performance of B-FNO against a variety of other well-known network structures. The first of these networks is CNN, which operates as a straightforward, forward-propagating, 4-layer convolutional neural network. This design can be distinguished for its simplicity and fluency in handling the feedforward mechanism. Next, we consider the ResNet structure [34]. This configuration comprises 4 residual blocks, with each block made up of two convolutional layers and a residual connection. The key feature of ResNet lies in the introduction of residual blocks, enabling the network to learn from the residuals or error terms, which tends to improve overall accuracy over time. Lastly, we examine the U-Net structure [35]. This is a unique network architecture that has been extensively employed in solving physical problems. It performs 5 layers of down-sampling via convolution, followed by sequential up-sampling. Notable for its "U" shaped structure, U-net excels at various tasks by capturing both high and low-level details through hierarchical feature learning. The 1D U-Net used an initial convolutional kernel size of 256, and 2D U-Net used an initial convolutional kernel size of 256×256.

To ensure a fair comparison, all four cases employ the same training and testing datasets, batch size, and optimization algorithm. Figure 13 plots the training loss curves for various networks in the context of elliptical scattering problems, 2D HR scattering problems, and 3D scattering problems with 2 by 2 arranged HRs. The figure also displays the average testing errors for all networks. The results demonstrate that, given the same number of training data

and epochs, B-FNO consistently outperforms the other three networks across all cases. B-FNO exhibits the highest convergence rate and accuracy, followed by U-Net. Plain CNN performs the least effectively. In particular, the performance of CNN and ResNet significantly deteriorates in more complex problems involving Helmholtz resonators. In contrast, the performance of B-FNO remains nearly unchanged in HR problems, highlighting its ability to capture wave physics, likely due to the non-local integral operation incorporated in its Fourier layers.

The training time of neural network models is influenced by multitude factors, which makes a comparative analysis challenging when controlling variables. As shown in Table 4, the training times per epoch of CNN and ResNet models employed in this work are considerably faster than that of the U-Net and the B-FNO models. The U-Net model equipped with a large initial convolutional kernel size, exhibits comparable run time to that of B-FNO. The interference time of the 2D U-Net model is approximately 2.9 milliseconds, while the B-FNO has an inference time of around 4.2 milliseconds, as indicated in Fig. 13(d). It is important to note that B-FNO requires significantly fewer training data to achieve the same level of accuracy. This reduction in the amount of necessary training data leads to considerable time savings in data generation, which is often a costly and resource-intensive process.

The amount of memory required to establish each network model is listed in Table 4 as the Model memory. It is directly related to the number of parameters in the network. Table 4 also shows the memory consumption of the entire model training process, which includes the memory required to build the trainer. In the B-FNO, the number of parameters associated with the kernel R_φ is determined by the number of Fourier layers, the hidden channel dimension H, the problem dimension N_D and the number of Fourier modes N_{modes},

Structural change probelm of ellipse scattering

(a)

Frequency sweeping probelm of ellipse scattering

(b)

2D HR scattering with varied frequency & geometry

(c)

2x2 arranged 3D HRs scattering problem

(d)

Fig. 13 **a** Loss curve of the structural change problem of ellipse scattering **b** Loss curve of the frequency sweeping problem of ellipse scattering **c** Loss curve of 2D HR scattering with varied frequency and geometry **d** Loss curve of the 2 by 2 arranged 3D HRs scattering

Table 4 The number of parameters, GPU memory usage to build network, and the training time per epoch of different network structures for the structural change problem of ellipse scattering and the 2 by 2 arranged 3D HRs scattering problem

Network	Ellipse scattering				3D HRs scattering			
	Number of parameters	Model memory/ bytes	Training memory/ bytes	Time per epoch/ sec.	Number of parameters	Model memory/ bytes	Training memory/ bytes	Time per epoch/ sec.
CNN	375	18,432	50,688	0.08	6,051	40,448	138,752	2.25
ResNet	113,026	471,552	1,844,736	0.13	337,090	1,368,064	5,430,784	5.90
U-Net	2,110,722	9,056,256	34,447,872	0.23	10,012,162	40,461,312	161,526,272	7.65
B-FNO	1,553,122	6,215,680	26,610,688	0.21	32,149,314	134,974,464	531,443,712	7.09

which can be expressed as $O\left(TH^2N_{modes}^{N_D}\right)$. As a result, B-FNO demands substantial GPU memory, particularly for 2D problems. Further work should be carried out to reduce the memory consumption.

5 Comparison of B-FNO with other BEMs

In this section, the performance of B-FNO is compared with the Fast Multipole accelerated Boundary Element Method (FMM-BEM). Our focus is on the efficiency comparison. However, both the conventional BEM and the FMM-BEM are coded using Fortran and executed on a computer with CPUs. Meanwhile, the B-FNO is constructed on the PyTorch platform and implemented on GPUs. Given these distinct operational contexts, it is unfeasible to make a direct comparison of computational times. Consequently, our comparison takes the form of analyzing the number of iterations.

The first example used for efficiency comparison among the two methods is the 2D HR scattering problem, as outlined in Sect. 3.2. Extra efforts have been put to ensure that the accuracies of the two methods are comparable for a fair efficiency comparison. As shown in Fig. 14(a), the HR, with a neck width of 25 cm and a height of 30 cm, is subjected to a plane wave incident at 1106 Hz. This specific case is evaluated using the conventional BEM, FMM-BEM, and B-FNO. The convergence criteria for the iterative solver in FMM-BEM is set at 1×10^{-3} to obtain the same maximum error as that in B-FNO. The absolute pressure field surrounding the HR calculated by the conventional BEM serves as the ground-truth and is plotted in Fig. 14(a). Based on the ground-truth, absolute errors of the pressure fields computed by B-FNO and FMM-BEM are calculated and plotted in Fig. 14(b) and (c) respectively. The maximum error of both methods is 0.005. Despite sharing the same time complexity

$O(NlogN)$, FMM-BEM demands 15 iterations using the GMRES solver to reach the same level of precision at the frequency of 1106 Hz. In the meantime, B-FNO only requires 4 FFT processes.

Furthermore, it's noteworthy that with the increase in ka, the number of required generations sees a corresponding increase. However, B-FNO consistently mandates the operation of merely 4 layers of FFT process.

Next, the ellipse frequency sweeping problem discussed in Sect. 3.1, featuring a dimensionless wavenumber range from 37 to 73, is also tested using FMM-BEM. However, due to the frequency limitation of traditional FMM-BEM, we employ a newer FMM-BEM variant capable of handling high frequency scenarios, known as fast directional BEM [36]. Under a frequency of 1500hz, the scattering sound pressure of a plane wave scattered by an ellipse, with a half major-axis of 1.2 m and a half minor-axis of 0.8 m, is depicted in Fig. 15(a). This pressure field is calculated by the conventional BEM and serves as the ground-truth. To achieve the accuracy depicted in Fig. 15(c), fast directional BEM requires 25 iterations, as shown in Fig. 15(b). On the other hand, B-FNO still needs only 4 FFT processes and its accuracy is slightly higher than that of FMM-BEM.

Based on the previous two examples, we have observed that the number of iterations in FMM-BEM increases as the non-dimensional wavenumber grows, which is expected due to the ill-conditioned nature of its system matrix. To further investigate the relationship between the number of iterations and the wavenumber, we employ 3D fast directional BEM to calculate the scattering wave fields of the two 3D HR scatterers mentioned in Sect. 3.3. The results, along with those corresponding to 2D problems, are depicted in Fig. 16. Once again, we observe an increasing trend with the rising wavenumber. It is worth noting that the condition of the BEM system matrix also depends on the complexity of the structure. Therefore, not only does the iteration count increase with the wavenumber growth, but the ill-conditioned matrix resulting
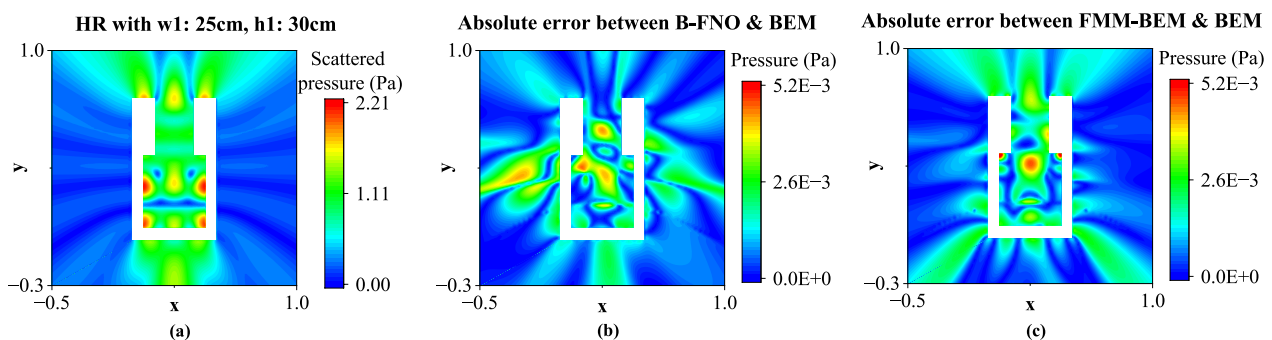

Fig. 14 a The absolute pressure scattered by the 2D HR with the width and height of the neck of 25 cm and 30 cm respectively at 1106 Hz. **b** The absolute error of scattered pressure between the results calculated by B-FNO & BEM. **c** The absolute error of scattered pressure between the results calculated by FMM-BEM & BEM
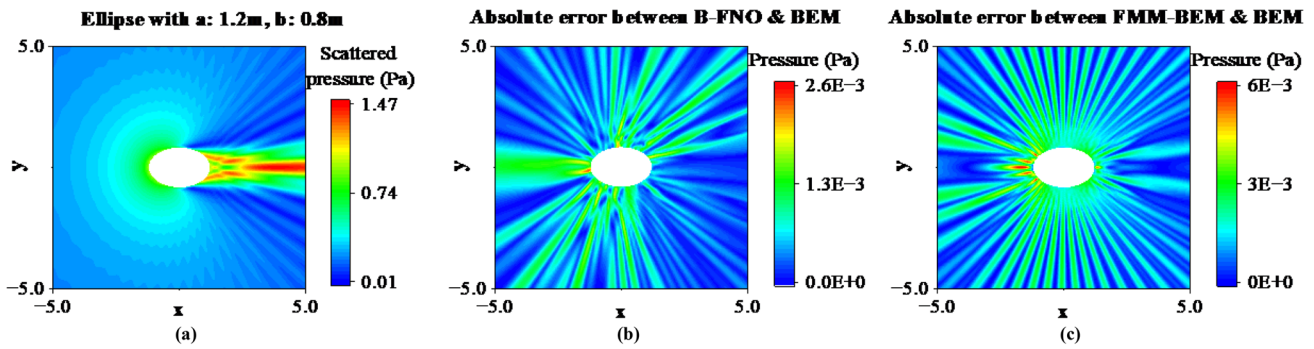
Fig. 15 a The absolute pressure scattered by the ellipse with the half major-axis of 1.2 m and the half minor-axis of 0.8 m at 1500 Hz. **b** The absolute error of scattered pressure between the results calcu- lated by B-FNO & BEM. **c** The absolute error of scattered pressure between the results calculated by FMM-BEM & BEM
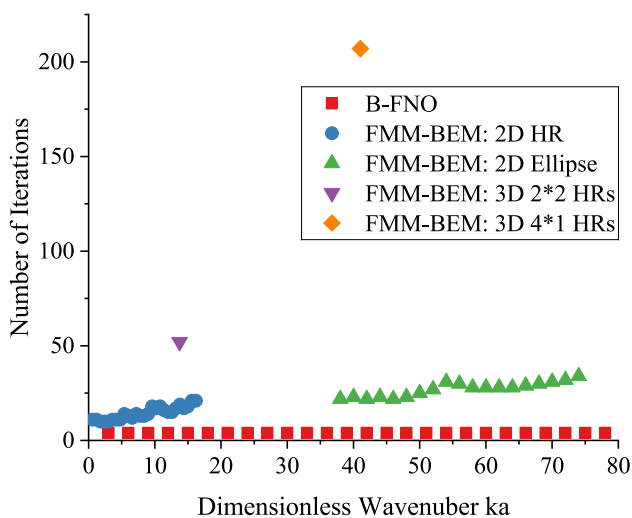
Fig. 16 The number of iterations varying with the dimensionless wavenumber for different numerical experiments

from complex structures can significantly amplify the number of iterations, as seen in the case of the 3D structure with linearly arranged HRs.

For comparison, we provide the number of FFT processes required in B-FNO in Fig. 16. In all cases, B-FNO utilizes only 4 layers of Fourier layers, resulting in 4 FFT processes, which demonstrates its distinct and significant iterative stability. Therefore, despite the $O(NlogN)$ time complexity of these methods, B-FNO holds its efficiency superiority due to its small and stable overhead.

6 Conclusions

In this paper, we introduce the B-FNO as a novel approach to addressing parametric acoustic wave analysis. By mapping the boundary of the problem and other physical parameters to the boundary solution space, the B-FNO has proven effective through various numerical experiments. These include tests on acoustic wave scattering from rigid ellipses and Helmholtz resonators, with cases spanning both two and three dimensions, as well as plane wave and point source incidences.

The results illustrate that B-FNO can be applied to a variety of structures and frequencies calculations. Further comparison with traditional BEM solvers, FMM-BEM solvers, and other neural network-based surrogate models highlight B-FNO's superior accuracy and efficiency.

The findings are in accord with recent studies indicating that FNO has an obvious advantage in predicting complex physical situations based on PDEs. While previous research has focused on modelling in a finite space, B-FNO contributes new insight into solving PDEs in an infinite space. Additionally, B-FNO reduces the problem dimension by one, thus enhancing the efficiency of the FNO.

One of our future works is to further improve the training and interference efficiency of B-FNO, as well as to reduce the memory usage. The time complexity caused by FFT in B-FNO is $O(NlogN)$, where N is the total number of boundary points. In light of this, we believe that there is significant room for efficiency and memory consumption improvements in three-dimensional problems through incorporating model-order-reduction techniques.

To date, our experiments have primarily revolved around scattering problems. Nonetheless, with a firm belief in its adaptability, we believe that B-FNO could be equally impactful in resolving radiation problems. Furthermore, the method should not be limited to acoustic wave analysis alone. It can be easily adapted to conduct elastic wave and electromagnetic wave analyses as well.

In conclusion, the B-FNO is a promising approach for parametric wave analysis, especially in infinite space that involve multiple structural simulations and frequency

sweeping problems. Further research is needed to explore the full potential of the B-FNO and to address any limitations that may arise.

Author contributions W.Y. conceived the idea. R.L. developed the approach and generated all results. R.L. and W. Y. performed analysis and drafted the manuscript. All authors reviewed and revised the manuscript.

Data availability Data will be provided upon request.

Declarations

Conflict of interest The authors declare no conflict of interest.

References

1. Rong J, Ye W (2020) Multifunctional elastic metasurface design with topology optimization. Acta Mater 185:382–399
2. Cheng H, Guo J, Zhang X, Ye W (2023) Frequency-multiplexed transmitted-wave manipulation with multifunctional acoustic metasurfaces. Phys Rev Appl 20(3):034009
3. Rokhlin V (1993) Diagonal forms of translation operators for the helmholtz equation in three dimensions. Appl Comput Harmon Anal 1(1):82–93
4. Rokhlin V (1990) Rapid solution of integral equations of scattering theory in two dimensions. J Comput Phys 86(2):414–439
5. Liu Y (2009) Fast Multipole Boundary Element Method: Theory and Applications in Engineering. Cambridge University Press
6. Brancati A, Aliabadi M, Benedetti I (2009) Hierarchical adaptive cross approximation GMRES technique for solution of acoustic problems using the boundary element method. Comput Model Eng Sci (CMES) 43(2):149
7. Xiao J, Ye W, Cai Y, Zhang J (2012) Precorrected FFT accelerated BEM for large-scale transient elastodynamic analysis using frequency-domain approach. Int J Numer Methods Eng 90(1):116–134
8. Amlani F, Chaillat S, Loseille A (2019) An efficient preconditioner for adaptive fast multipole accelerated boundary element methods to model time-harmonic 3D wave propagation. Comput Methods Appl Mech Eng 352:189–210
9. Panagiotopoulos D, Deckers E, Desmet W (2020) Krylov subspaces recycling based model order reduction for acoustic BEM systems and an error estimator. Comput Methods Appl Mech Eng 359:112755
10. Xie X, Liu Y (2021) An adaptive model order reduction method for boundary element-based multi-frequency acoustic wave problems. Comput Methods Appl Mech Eng 373:113532
11. Li Y, Atak O, Jonckheere S, Desmet W (2022) Accelerating boundary element methods in wideband frequency sweep analysis by matrix-free model order reduction. J Sound Vib 541:117323
12. Bacigalupo A, Gnecco G, Lepidi M, Gambarotta L (2020) Machine-learning techniques for the optimal design of acoustic metamaterials. J Optim Theory Appl 187:630–653
13. Donda K, Zhu Y, Merkel A, Fan S-W, Cao L et al (2021) Ultrathin acoustic absorbing metasurface based on deep learning approach. Smart Mater Struct 30(8):085003
14. Fan Z, Vineet V, Gamper H, Raghuvanshi N (Year) Fast acoustic scattering using convolutional neural networks (eds) In Proc. ICASSP 2020–2020 IEEE International Conference on Acoustics, Speech and Signal Processing (ICASSP) 2020, 171–175
15. Alguacil A, Bauerheim M, Jacob MC, Moreau S (2021) Predicting the propagation of acoustic waves using deep convolutional neural networks. J Sound Vib 512:116285
16. Zhang H, Wang Y, Zhao H, Lu K, Yu D et al (2021) Accelerated topological design of metaporous materials of broadband sound absorption performance by generative adversarial networks. Mater Design 207:109855
17. Gurbuz C, Kronowetter F, Dietz C, Eser M, Schmid J et al (2021) Generative adversarial networks for the design of acoustic metamaterials. J Acoust Soc Am 149(2):1162–1174
18. Lai P, Amirkulova F, Gerstoft P (2021) Conditional Wasserstein generative adversarial networks applied to acoustic metamaterial design. J Acoust Soc Am 150(6):4362–4374
19. Raissi M, Perdikaris P, Karniadakis GE (2019) Physics-informed neural networks: a deep learning framework for solving forward and inverse problems involving nonlinear partial differential equations. J Comput Phys 378:686–707
20. Cai S, Mao Z, Wang Z, Yin M, Karniadakis GE (2021) Physics-informed neural networks (PINNs) for fluid mechanics: a review. Acta Mech Sin 37(12):1727–1738
21. Krishnapriyan A, Gholami A, Zhe S, Kirby R, Mahoney MW (2021) Characterizing possible failure modes in physics-informed neural networks. Adv Neural Inf Process Syst 34:26548–26560
22. Sun J, Liu Y, Wang Y, Yao Z, Zheng X (2023) BINN: a deep learning approach for computational mechanics problems based on boundary integral equations. Comput Methods Appl Mech Eng 410:116012
23. Lu L, Jin P, Pang G, Zhang Z, Karniadakis GE (2021) Learning nonlinear operators via DeepONet based on the universal approximation theorem of operators. Nat Mach Intell 3(3):218–229
24. Patel RG, Trask NA, Wood MA, Cyr EC (2021) A physics-informed operator regression framework for extracting data-driven continuum models. Comput Methods Appl Mech Eng 373:113500
25. Bhattacharya K, Hosseini B, Kovachki NB, Stuart AM (2021) Model reduction and neural networks for parametric PDEs. SMAI J Comput Math 7:121–157
26. Li Z, Kovachki N, Azizzadenesheli K, Liu B, Bhattacharya K et al (2020) Fourier neural operator for parametric partial differential equations. arXiv preprint arXiv:201008895
27. Li Z, Kovachki N, Azizzadenesheli K, Liu B, Stuart A et al (2020) Multipole graph neural operator for parametric partial differential equations. Adv Neural Inf Process Syst 33:6755–6766
28. Lehmann F, Gatti F, Bertin M, Clouteau D (2024) 3D elastic wave propagation with a factorized Fourier neural operator (F-FNO). Comput Methods Appl Mech Eng 420:116718

29. Tran A, Mathews A, Xie L, Ong CS (2021) Factorized fourier neural operators. arXiv preprint arXiv:211113802

30. Li B, Wang H, Feng S, Yang X, Lin Y (2023) Solving seismic wave equations on variable velocity models with fourier neural operator. IEEE Trans Geosci Remote Sens 61:1–18

31. Zhu M, Feng S, Lin Y, Lu L (2023) Fourier-DeepONet: Fourier-enhanced deep operator networks for full waveform inversion with improved accuracy, generalizability, and robustness. Comput Methods Appl Mech Eng 416:116300

32. Burton A, Miller G (1971) The application of integral equation methods to the numerical solution of some exterior boundary-value problems. Proc Royal Soc Lond Math Phys Sci 323(1553):201–210

33. Saad Y, Schultz MH (1986) GMRES: a generalized minimal residual algorithm for solving nonsymmetric linear systems. SIAM J Sci Stat Comput 7(3):856–869

34. He K, Zhang X, Ren S, Sun J (2015) Deep Residual Learning for Image Recognition. arXiv preprint arXiv:151203385

35. Ronneberger O, Fischer P, Brox T (2015) U-Net: Convolutional Networks for Biomedical Image Segmentation. arXiv preprint arXiv:150504597

36. Cao Y, Wen L, Xiao J, Liu Y (2015) A fast directional BEM for large-scale acoustic problems based on the burton–miller formulation. Eng Anal Boundary Elem 50:47–58